Isolating Bandpass Filters Using Time-Modulated Resonators

Xiaohu Wu, *Member, IEEE,* Xiaoguang Liu, *Senior Member, IEEE,* Mark D. Hickle, *Member, IEEE,*
Dimitrios Peroulis, *Fellow, IEEE,* J. Sebastián Gómez-Díaz, *Senior Member, IEEE,*
and Alejandro Álvarez Melcón, *Senior Member, IEEE*

Abstract—In this paper, we demonstrate for the first time an isolating bandpass filter with low-loss forward transmission and high reverse isolation by modulating its constituent resonators. To understand the operating principle behind the device, we develop a spectral domain analysis method and show that same-frequency non-reciprocity is a result of non-reciprocal frequency conversion to the intermodulation (IM) frequencies by the time-varying resonators. With appropriate modulation frequency, modulation depth, and phase delay, the signal power at the IM frequencies is converted back to the RF frequency and add up constructively to form a low-loss forward passband, whereas they add up destructively in the reverse direction to create the isolation. To validate the theory, a lumped-element 3-pole 0.04-dB ripple isolating filter with a center frequency of 200 MHz, a ripple bandwidth of 30 MHz, is designed, simulated, and measured. When modulated with a sinusoidal frequency of 30 MHz, a modulation index of 0.25, and an incremental phase difference of $45°$, the filter achieves a forward insertion loss of 1.5 dB and a reverse isolation of 20 dB. The measured non-modulated and modulated results agree very well with the simulations. Such non-reciprocal filters may find applications in wide-band simultaneous transmit and receive radio front-ends.

Index Terms—Bandpass filter (BPF), isolator, non-reciprocity, spatio-temporal modulation (STM), time-invariant, time-modulated, time-varying.

I. INTRODUCTION

X. Wu is with the School of Electronic and Information Engineering, Nanjing University of Information Science and Technology, Nanjing, China, and also with the Department of Electrical and Computer Engineering, University of California, Davis, USA. e-mail: xiaohu.wu@nuist.edu.cn, wxhwu@ucdavis.edu

M. D. Hickle was with the School of Electrical and Computer Engineering, Purdue University, West Lafayette, IN 47907 USA. He is now with BAE Systems, Inc., Merrimack, NH 03054 USA. e-mail: mark.hickle@baesystems.com

D. Peroulis is with the School of Electrical and Computer Engineering, Purdue University, West Lafayette, USA. e-mail: dperouli@purdue.edu

J. S. Gómez-Díaz and X. Liu are with the Department of Electrical and Computer Engineering, University of California, Davis, USA. e-mail: jsgomez, lxgliu@ucdavis.edu

A. A. Melcón is with the Department of Information and Communication Technologies, Technical University of Cartagena, Murcia, 30202, Spain. e-mail: alejandro.alvarez@upct.es

NON-RECIPROCAL microwave components, such as circulators, isolators, and gyrators, are important building blocks in many wireless systems to prevent undesirable reflections [1]. They can also be used to allow transmitting and receiving simultaneously at the same frequency, thereby increasing the channel capacity without requiring more bandwidth [2]–[5]. In general, a linear time-invariant circuit consisting of materials with symmetric electric permittivity and magnetic permeability tensors is reciprocal. To achieve non-reciprocity, one of these conditions must be circumvented [6].

Traditionally, non-reciprocal components are constructed using magnetic materials in which the internal magnetic moment of the material breaks the reciprocity when biased with a static magnetic field [7]–[11]. However, magnetic circulators and isolators are generally bulky and expensive. As an ever increasing number of functionality of a microwave system is now realized in integrated circuit (IC) form, circulators and isolators remain a bottleneck of integration.

To overcome the integration issue, non-reciprocity has been attempted by using active devices such as transistors. Non-reciprocal circuits in discrete form [12]–[14] or embedded within metamaterials [15] have been demonstrated. However, active devices based circulators/isolators generally suffer from poor noise figure, limited power handling, and therefore yield a moderate/low dynamic range [16]. In addition, broadband power-dependent non-reciprocity has been demonstrated in [17], by combining nonlinear Lorentzian and Fano resonators with certain type of delay lines, an approach limited to a range of high intensity signals exciting a single port at the time.

Recently, magnetless non-reciprocal devices based on time-varying circuits have received significant attention. The intensity-independent modulation provides great design flexibility, which has allowed researchers to put forward a wide variety of magnetless non-reciprocal devices in electromagnetics and acoustics [18]–[21]. In [21], a transmission line periodically loaded with time-varying capacitors is shown to exhibit non-reciprocity. The capacitors are modulated by a sinusoidal signal with a progressive delay. Since the modulation is both time and location dependent, the modulation scheme is referred to as "spatio-temporal" modulation (STM). Non-reciprocity in [21] is observed from the RF carrier to the mixing products, and a frequency diplexer is used to separate the signals traveling in opposite directions. In the implementation, a relatively long loaded transmission line of $3.9\lambda_g$ and a modulation frequency higher than the RF

frequency are needed, both of which present challenges in miniaturization and power consumption.

Non-reciprocity can also be realized by using the angular-momentum biasing in a ring or loop structure to mimic the Faraday effect in magnetic materials. In [22], circulating the fluid physically in a resonant ring cavity splits the ring's azimuthal resonant modes and produce significant acoustic non-reciprocity. In the electronic domain, STM has been used to achieve angular-momentum biasing and non-reciprocity [23]–[29]. For example, in [23], angular momentum-biased devices are presented in a ring structure with continuous capacitive loading. STM is introduced across the transverse surface area of the ring, leading to an effective electric rotation and strong non-reciprocity at the sub-wavelength scale. In [24], composite loop of three discrete shunt resonators in a Δ topology is presented. The resonant frequencies of the three resonators are modulated in time with $120°$ phase difference between each other. Deep isolation can be generated with a small modulation index and a modulation frequency of 20%–30% of the RF carrier frequency. In [25], three series resonators are connected in a Y topology to simplify the bias circuit. Three film bulk acoustic resonators (FBAR) in [27] and MEMs resonators in [28] are used in the same fashion to achieve non-reciprocity with a very small modulation frequency. Differential circulators are presented in [28]–[30] to cancel the undesired intermodulation products, which helps to improve the insertion loss, impedance matching, bandwidth, and noise figure. Three identical BPFs are used to broaden the isolation bandwidth of such spatiotemporally modulated circulator in [31].

In [32], ultra-wideband non-reciprocity is achieved by sequentially switching between the transmission and receiving paths. Specifically, six transmission lines of equal length and five single-pole double-throw switches are used to construct the circuit. The switch timing is synchronized with the delay in the transmission lines. In [33]–[35], gyrators with $\pm\pi/2$ phase non-reciprocity are realized through staggered commutation inside N-path filters. Based on the same principle, two double-pole double-throw switches with $\lambda/4$ delay lines are properly synchronized to have non-reciprocity not only in phase but also in magnitude [36]. Approaches based on commutated gyrators are compact in size and compatible with integrated-circuit fabrication. However, they require switching frequency to be the same as the center frequency of the non-reciprocal devices, leading to challenges in power consumption and suppressing clock leakage.

In this paper, we report the design of novel non-reciprocal bandpass filters that allow signal to travel in only one direction using the STM principle, realizing an isolator and a bandpass filter integrated in one device. Fig. 1 captures the concept of this "isolating filter" which consists of a series of coupled resonators that are temporally modulated [37]. To understand the creation of non-reciprocity in such a structure, we utilize the spectral domain method to analyze the time-varying circuit. Essentially, each time-varying component in the circuit produces intermodulation (IM) products. It can be shown that energy conversion between the carrier and the IM frequencies is non-reciprocal whereas energy transmission at the carrier frequency only is strictly reciprocal. We demonstrate that
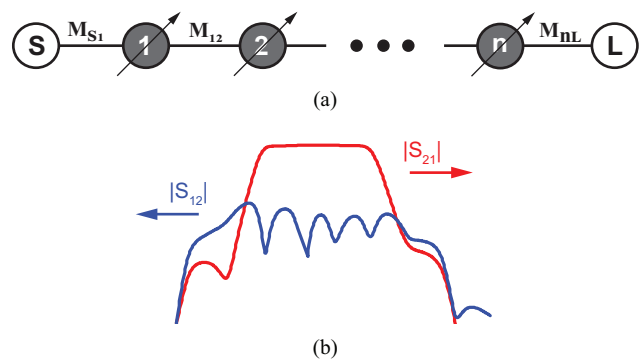

Fig. 1. (a) Topology diagram of the proposed time-modulated isolating filter Black circles with arrow: time-modulated resonator with the angular frequency defined as $\omega_i = \omega_0 \{1 + \xi \cos [\omega_m t + (i - 1)\Delta\phi]\}$, $i = 1, 2, \ldots, N$; white circles: unitary source (S) and load (L); M_{S1}: coupling between source and resonator 1; M_{nL}: coupling between resonator n and load. (b) Non-reciprocal forward transmission $|S_{21}|$ and backward transmission $|S_{12}|$, where port 1 refers to the source and port 2 refers to the load.

same-frequency non-reciprocity at the carrier frequency can be achieved with low insertion loss in higher order modulated filters. We show that this is due to the additional degrees of freedom available with more time-varying elements to enable that non-reciprocal IM signals can be converted back to the transmission of carrier frequency. As an experimental validation, a 3-pole isolating filter is demonstrated to exhibit flat in-band transmission, low insertion loss ($1.5\,\text{dB}$), high reverse isolation ($20\,\text{dB}$), and good matching ($15\,\text{dB}$) at both ports. To the authors' knowledge, this is the first report of a 2-port isolating circuit that exhibits strong same-frequency non-reciprocity.

This paper is organized as follows. Section II reviews the spectral domain analysis techniques for time-varying circuits and presents the full-spectral matrix theory for the most general form of spatio-temporal modulated circuits. Section III presents the full-spectral matrix analysis for filters, including single resonator, 2-pole filter, and 3-pole filter. The numerical convergence is also discussed. Section IV presents the design of a 3-pole isolating filter and its simulation and measurement results. Finally, the conclusions are given in Section V.

II. ANALYSIS OF TIME-VARYING CIRCUITS

The analysis of linear time-varying (LTV) circuits with time-harmonic variations is well understood with the spectral domain method [38]. To set the background for further analysis, this section presents a *review* of such method and based on the newly defined multi-dimensional full spectral matrix, the full spectral network parameter matrices are developed and expanded to consider devices composed of any number of time-modulated resonators, yielding to a rigorous spectral domain approach able to characterize energy transmission and reflection in general time-varying networks.

Fig. 2 shows a basic LTV circuit with a single shunt time-varying capacitor $C(t)$. V_S is the source with source impedance R_S located at the left port (port 1) and a resistor terminal R_L is located at the right port (port 2). R_S and R_L
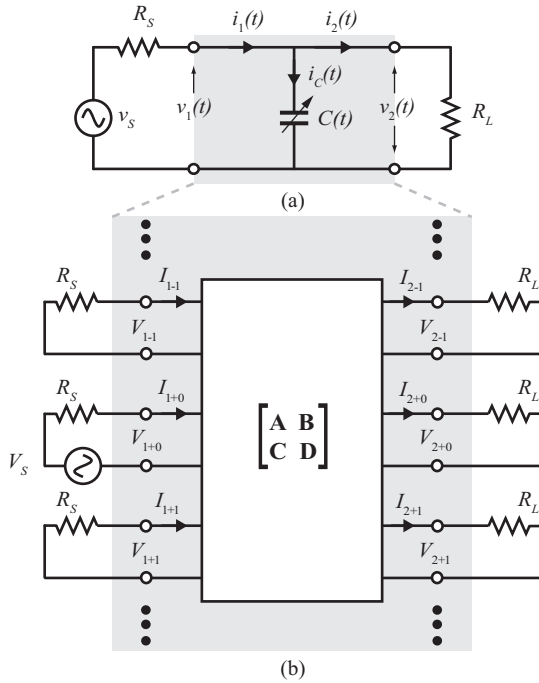
Fig. 2. (a) A simple linear time-varying circuit with a single sinusoidally modulated shunt capacitor. (b) A general spectral equivalent circuit contains ports for all the intermodulation frequencies.

are time-invariant and frequency independent. The variation of the capacitor is assumed to be time harmonic, i.e.,

$$C(t) = C_0 + \Delta C \cos\left(\omega_m t + \phi\right), \tag{1}$$

where C_0 is the nominal (dc) capacitance, ΔC is the modulation depth, ω_m is the modulation angular frequency, and ϕ is the phase shift of the modulating waveform. A modulation index parameter ξ is defined as

$$\xi = \frac{\Delta C}{C_0}. \tag{2}$$

The voltages and currents of the two-port network consisting of a shunt capacitor only are related by

$$v_1(t) = v_2(t), \tag{3a}$$

$$\int_0^t i_1(\tau)d\tau = C(t)v_2(t) + \int_0^t i_2(\tau)d\tau. \tag{3b}$$

Since the modulation is periodic, we can represent (3) in the frequency domain by its Fourier series. Note that the port voltages and currents should contain not only the RF carrier signal at ω but also all the IM products at $\omega \pm n\omega_m$ ($n = 0, 1, 2, \ldots$) which are due to the sinusoidal modulation of the capacitor [38]. The spectral frequency matrix $\boldsymbol{\omega}$ is defined to capture all the spectral frequencies in the time-varying circuits, where all the off-diagonal elements are zero

$$\boldsymbol{\omega} = \text{diag}\left(\ldots, \omega - 2\omega_m, \omega - \omega_m, \omega, \omega + \omega_m, \ \omega + 2\omega_m, \ldots\right). \tag{4}$$

Therefore, in the frequency domain, the port voltages and currents take the form of vectors, viz., $\boldsymbol{V_i} = [\ldots, V_{i-2}, V_{i-1}, V_{i+0}, V_{i+1}, V_{i+2}, \ldots]$ and $\boldsymbol{I_i} = [\ldots, I_{i-2}, I_{i-1}, I_{i+0}, I_{i+1}, I_{i+2}, \ldots]$. Here, $V_{i\pm n}$ and

$I_{i\pm n}$ ($i = 1, 2$, $n = \mathbb{Z}$) are the phasor representation of the voltage and current of port i at frequency $\omega \pm n\omega_m$, respectively.

The frequency domain form of (3) is then

$$\begin{bmatrix} V_1 \\ I_1 \end{bmatrix} = \begin{bmatrix} \mathbf{U} & \mathbf{0} \\ \mathbf{Y_C} & \mathbf{U} \end{bmatrix} \begin{bmatrix} V_2 \\ I_2 \end{bmatrix}, \tag{5}$$

where $\mathbf{0}$ is the zero matrix, $\mathbf{U}$ is the unity matrix, and $\mathbf{Y_C}$ is the spectral admittance matrix of the shunt time-varying capacitor, as given in (6), which is shown in the next page. It should be noted that (5) also reveals the spectral $\mathbf{ABCD}$ matrix of the temporally modulated capacitor. Theoretically, the dimensions of $\mathbf{0}$, $\mathbf{U}$, and $\mathbf{Y_C}$ are infinite because the modulation of the capacitor generates infinite number of IM products at frequencies $\omega \pm n\omega_m$. In practice, only a limited number of IM products need to be considered for a given accuracy requirement.

To make the notation more intuitive, we base the element indices of $\mathbf{Y_C}$ in the center of the matrix and use them to indicate the frequency, i.e., $Y_{C,(\pm n_1, \pm n_2)}$ represents the admittance/transconductance from frequency $\omega \pm n_1\omega_m$ to frequency $\omega \pm n_2\omega_m$. The diagonal elements $Y_{C,(\pm n_1, \pm n_1)}$ correspond to the admittance of the time-varying capacitor at each IM frequency. The off-diagonal elements $Y_{C,(\pm n_1, \pm n_2)}$ ($n_1 \neq n_2$) correspond to the transconductance from frequency $\omega \pm n_1\omega_m$ to frequency $\omega \pm n_2\omega_m$.

It is clear from (6) that $Y_{C,(n_1, n_2)}$ and $Y_{C,(n_2, n_1)}$ ($n_1 \neq n_2$) are not equal to each other. For example,

$$Y_{C,(-1,0)} = (\omega - \omega_m)\frac{\xi}{2}e^{-j\phi} \tag{7}$$

whereas

$$Y_{C,(0,-1)} = \omega\frac{\xi}{2}e^{j\phi}. \tag{8}$$

There is not only a difference in the magnitude, but also a difference in the phase when $\phi \neq 0$. Although the simple circuit with only one time-varying element exhibits no non-reciprocity at the RF carrier frequency, this asymmetry in the transconductance between a pair of IM frequencies forms the basis of the non-reciprocal behavior achieved in our proposed isolating filter.

Eq. (5) and (6) indicate that the RF carrier at ω is up-converted and down-converted to all the IM frequencies by the time-varying capacitor. As such, an equivalent circuit of the capacitor must contain ports for all the IM frequencies, as shown in Fig. 2 (b). By exploring the network parameters in the defined full spectral matrix space, a more comprehensive solution can be derived from (5) and the general equivalent circuit of Fig. 2 (b) to illustrate the energy transmission and reflection among all the spectral frequencies. The S-parameters of the two-port network representing the time-varying capacitor are shown in (9). The detailed procedures of the derivation are given in the Appendix. Note that each $\mathbf{S_{ij}}$ is a matrix of similar dimensions as $\mathbf{Y_C}$ to represent the interactions between different IM frequencies.

To validate the presented full-spectral analysis, we present in Fig. 3 the simulated and calculated S-parameters of the

$$\mathbf{Y_C} = jC_0 \begin{bmatrix} \ddots & \vdots & \vdots & \vdots & \vdots & \vdots & \cdot^{\cdot^\cdot} \\ \cdots & (\omega - 2\omega_m) & (\omega - 2\omega_m)\frac{\xi}{2}e^{-j\phi} & 0 & 0 & 0 & \cdots \\ \cdots & (\omega - \omega_m)\frac{\xi}{2}e^{j\phi} & (\omega - \omega_m) & (\omega - \omega_m)\frac{\xi}{2}e^{-j\phi} & 0 & 0 & \cdots \\ \cdots & 0 & \omega\frac{\xi}{2}e^{j\phi} & \omega & \omega\frac{\xi}{2}e^{-j\phi} & 0 & \cdots \\ \cdots & 0 & 0 & (\omega + \omega_m)\frac{\xi}{2}e^{j\phi} & (\omega + \omega_m) & (\omega + \omega_m)\frac{\xi}{2}e^{-j\phi} & \cdots \\ \cdots & 0 & 0 & 0 & (\omega + 2\omega_m)\frac{\xi}{2}e^{j\phi} & (\omega + 2\omega_m) & \cdots \\ \cdot^{\cdot^\cdot} & \vdots & \vdots & \vdots & \vdots & \vdots & \ddots \end{bmatrix} \cdot \begin{matrix} \vdots \\ \mathbf{-2} \\ \mathbf{-1} \\ \mathbf{0} \\ \mathbf{+1} \\ \mathbf{+2} \\ \vdots \end{matrix} \qquad (6)$$

with column indices $\cdots \; \mathbf{-2} \; \mathbf{-1} \; \mathbf{0} \; \mathbf{+1} \; \mathbf{+2} \; \cdots \; \mathbf{indices}$

$$\begin{bmatrix} \mathbf{S_{11}} & \mathbf{S_{12}} \\ \mathbf{S_{21}} & \mathbf{S_{22}} \end{bmatrix} = \begin{bmatrix} \mathbf{U} - 2[\mathbf{U} + (\mathbf{A}R_2 + \mathbf{B})(\mathbf{C}R_1R_2 + \mathbf{D}R_1)^{-1}]^{-1} & \begin{matrix} 2[\mathbf{U} + (\mathbf{A}R_2 + \mathbf{B})(\mathbf{C}R_2 + \mathbf{D})^{-1}/R_1]^{-1} \\ \times[\mathbf{A} - (\mathbf{A}R_2 + \mathbf{B})(\mathbf{C}R_2 + \mathbf{D})^{-1}\mathbf{C}] \end{matrix} \\ 2\sqrt{\dfrac{R_S}{R_L}}[\mathbf{A} + \mathbf{B}/R_2 + \mathbf{C}R_1 + \mathbf{D}R_1/R_2]^{-1} & \mathbf{U} - 2[\mathbf{U} + (\mathbf{A}R_2 + \mathbf{C}R_1R_2)^{-1}(\mathbf{B} + \mathbf{D}R_1)]^{-1} \end{bmatrix} . \qquad (9)$$
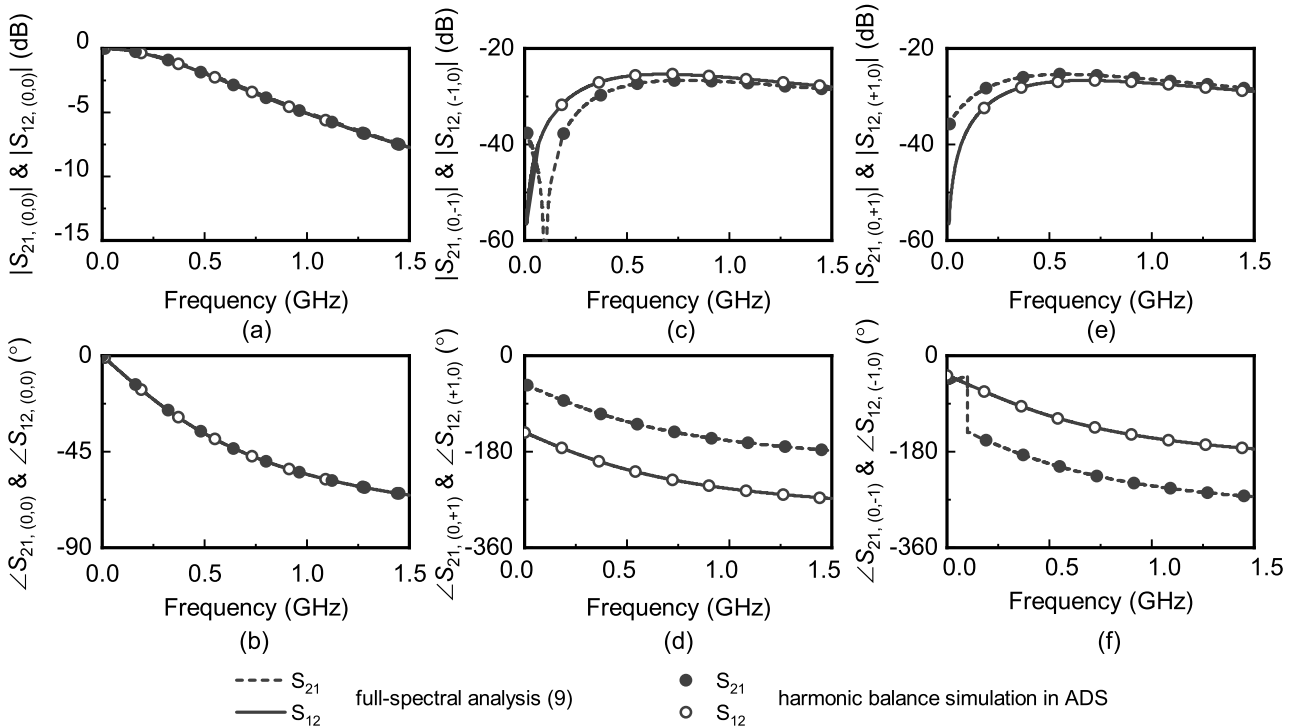

Fig. 3. Synthesized and simulated transmission properties of a single time-varying capacitor in Fig. 2. (a) $|S_{21,(0,0)}|$ and $|S_{12,(0,0)}|$. (b) $\angle S_{21,(0,-2)}$ and $\angle S_{12,(0,-2)}$. (c) $|S_{21,(0,+1)}|$ and $|S_{12,(+1,0)}|$. (d) $\angle S_{21,(0,+1)}$ and $\angle S_{12,(+1,0)}$. (e) $|S_{21,(0,-1)}|$ and $|S_{12,(-1,0)}|$. (f) $\angle S_{21,(0,-1)}$ and $\angle S_{12,(-1,0)}$.

circuit in Fig. 2 (a). Here, the source and load impedances are both set to be $50\,\Omega$. The time-varying capacitance has a nominal value of $9.6\,\text{pF}$, and a modulation index of $\xi = 0.2$, modulation frequency of $f_m = 100\,\text{MHz}$, and a starting phase of $\phi_0 = 45°$.

Fig. 3 (a) and (b) shows the transmission between the RF carrier frequency ω at port 1 and ω at port 2, denoted by $S_{21,(0,0)}$ and $S_{12,(0,0)}$. Here, we follow the same index notation of $\mathbf{Y_C}$ as in (6) for the S-parameters. As expected, the circuit is reciprocal at ω. The full-spectral solution of (9) agrees exactly
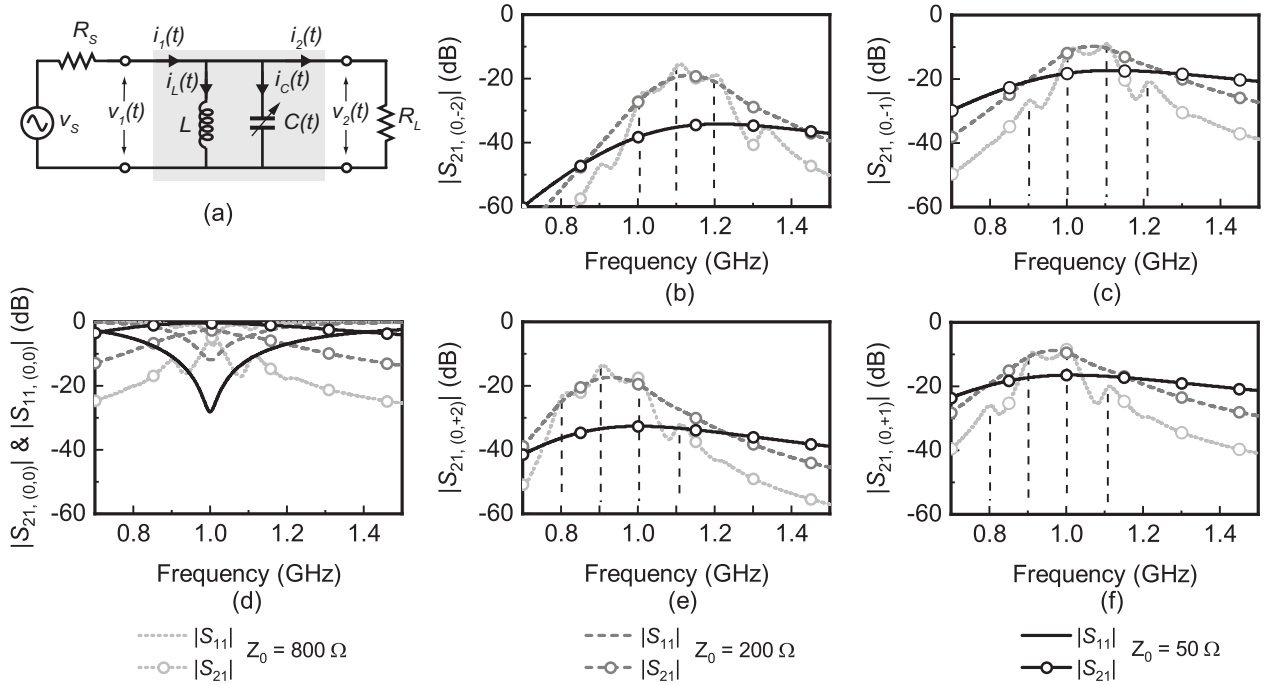
Fig. 4. (a) Shunt LC resonator with time-invariant inductor L and time-varying capacitor $C(t)$. (b) $|S_{21,(0,-2)}|$. (c) $|S_{21,(0,-1)}|$. (d) $|S_{21,(0,0)}|$. (e) $|S_{21,(0,+2)}|$. (f) $|S_{21,(0,+1)}|$.

with the harmonic balance simulation in Keysight Advanced Design System (ADS). Fig. 3 (c) and (d) show the transmission between ω and $\omega - \omega_m$ ($S_{21,(0,-1)}$ and $S_{12,(0,-1)}$). A non-reciprocal behavior is clearly observed in both magnitude and phase. Note that the phase difference between $S_{21,(0,-1)}$ and $S_{12,(0,-1)}$ is exactly $90°$ (2ϕ). Similar behaviors are observed for the transmission between ω and $\omega + \omega_m$, as shown in Fig. 3 (e) and (f). Consequently, the full-spectral method of (9) will be used through out the paper to analyze time-varying circuits.

III. TIME-VARYING RESONATORS AND FILTERS

A. Time-Modulated Resonator

The analysis presented in Section II can be extended to time-varying resonators which form the building blocks of many STM circuits [25]. Fig. 4 (a) shows a simple shunt time-varying LC resonator consisting of a time-invariant inductor L and a time-varying capacitor $C(t)$. The spectral admittance of the shunt time-varying LC resonator is simply $\mathbf{Y_{LC}} = \mathbf{Y_L} + \mathbf{Y_C}$, where $\mathbf{Y_L} = (j\boldsymbol{\omega}L)^{-1}$ is the spectral admittance of L. Here $\boldsymbol{\omega}$ is the diagonal frequency matrix given by (4). Thus, the spectral $\mathbf{ABCD}$ matrix of the time-varying resonator is

$$\mathbf{N_{LC}} = \begin{bmatrix} \mathbf{U} & \mathbf{0} \\ \mathbf{Y_{LC}} & \mathbf{U} \end{bmatrix}. \tag{10}$$

The performance of the circuit may be solved in a similar fashion as in (9). Fig. 4 (b)–(f) show the simulated transmission from ω to $\omega - 2\omega_m$ ($S_{21,(0,-2)}$), from ω to $\omega - \omega_m$ ($S_{21,(0,-1)}$), from ω to ω ($S_{21,(0,0)}$), from ω to $\omega + 2\omega_m$ ($S_{21,(0,+2)}$),

and from ω to $\omega + \omega_m$ ($S_{21,(0,+1)}$), respectively. The power reflection from ω to ω ($S_{11,(0,0)}$ is also inserted in Fig. 4 (d). Since the power reflected from ω to $\omega \pm n\omega_m$ ($S_{11,(0,\pm n)}$) are exactly the same as the power transmitted from ω to $\omega \pm n\omega_m$ ($S_{21,(0,\pm n)}$) for a single shunt time-varying resonator, thus $S_{11,(0,\pm n)}$ is not shown in Fig. 4 (b), (c), (e), and (f). Here, the time-varying capacitance has a nominal value of $9.6\,\mathrm{pF}$ which resonates with a static inductor of $2.6\,\mathrm{nH}$ at $1\,\mathrm{GHz}$. Modulation is applied to the capacitor with $f_m = 100\,\mathrm{MHz}$, $\xi = 0.2$, and $\phi_0 = 45°$.

A few observations can be made. First, the transmission is a strong function of the port impedances ($R_S = R_L$) seen by the resonator. Around the static center frequency of $1\,\mathrm{GHz}$, the transmission at ω decreases whereas the transmission from ω to the IM frequencies increases, as R_S (R_L) increases. A qualitative explanation for this is that $C(t)$ is effectively shorted by R_S (R_L) when R_S (R_L) is small compared to $1/j\omega C(t)$. As a result, the effect of the modulation is small and most of the available source power is delivered to the load.

When R_S (R_L) is larger, the effect of the capacitance modulation is stronger. More power is converted to the IM frequencies and as a result, the transmission at ω becomes weaker. As R_S (R_L) increases, the effective loaded quality factor Q_L at ω and the IM frequencies increases, as is the case for static resonators. The higher Q_L allows us to observe the frequency translation characteristics of the circuit; distinctive peaks at IM frequencies can be observed in the transmission between frequencies.

When time-varying resonator is used in a more complicated circuit, such as the STM circulator [25] and filter presented later in this work, the impedances presented to the resonator may vary over a large range depending on the strength of the
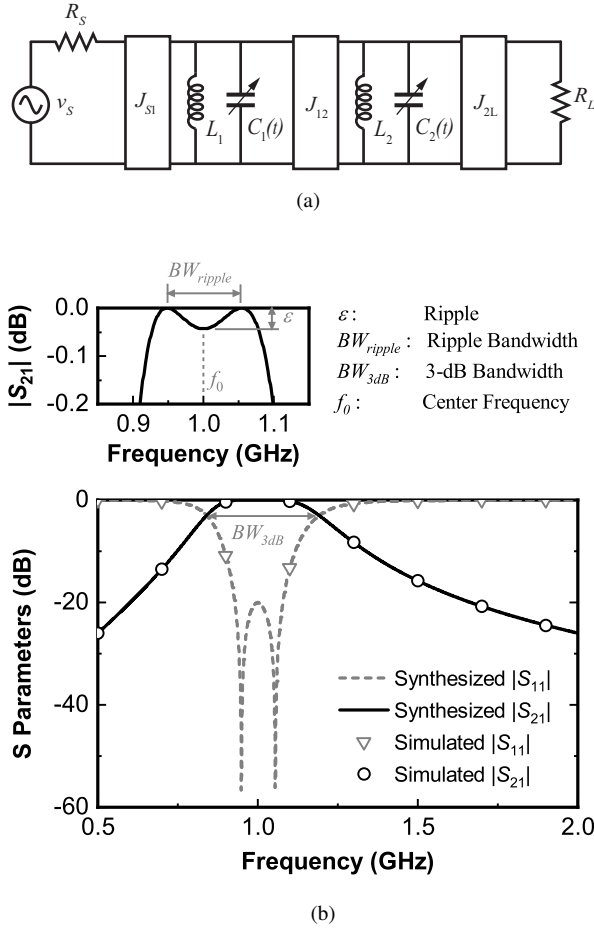
(a)

(b)

Fig. 5. (a) Topology of the 2nd order spatio-temporally modulated filter. (b) Simulated responses of non-modulated 2-pole BPF ($J_{S1} = J_{2L} = 0.0134\,\Omega^{-1}$, $J_{12} = 0.01\,\Omega^{-1}$, $R_S = R_L = 50\,\Omega$, $L_1 = 4\,\text{nH}$, $L_2 = 4\,\text{nH}$, $C_{01} = 6.37\,\text{pF}$, and $C_{02} = 6.37\,\text{pF}$).

couplings between the resonators. As a result, a significant portion of the power may be converted to and back from the IM frequencies to create non-reciprocal transmission characteristics.

B. Filters—Introducing Spatial Modulation

From the above analysis, we have seen that for time-varying circuits containing only one time-varying component, non-reciprocity can not be observed at the RF carrier frequency, although the conversion between different frequencies is non-reciprocal. To achieve same-frequency non-reciprocity, more than one time-varying component is needed. The rationale is illustrated qualitatively in Fig. 4.

With one time-varying component, the available power from the carrier frequency is spread among the carrier frequency and all the IM frequencies. The power that is transmitted and reflected to the IM frequencies shows up as loss when we consider the transmission at the carrier frequency ($S_{21,(0,0)}$). When more time-varying components are added to the system, the transmitted and reflected IM products may be up- and down-converted back to the carrier frequency. Because $S_{21,(0,0)}$ now contains contributions from frequency translation, and that frequency translation is non-reciprocal,

$S_{21,(0,0)}$ may become non-reciprocal as well. More importantly, under the right modulation parameters, the power at the IM frequencies may be collected back at the carrier frequency constructively and a low insertion loss may be achieved.

To demonstrate this, we first study the behavior of a 2-pole filter composed of dual time-varying resonators. Fig. 5 shows the circuit topology of the 2-pole filter. Here, ideal admittance inverters are used to realize inter-resonator and external couplings. The two resonators are modulated by modulating the capacitors as follows

$$C_i(t) = C_{0i}\left[1 + \xi_i \cos\left(\omega_{mi}t + \phi_i\right)\right], \quad i = 1,\, 2. \tag{11}$$

In general, the modulation conditions for the two resonators are different not only in time but also in space, and hence the notion "spatio-temporal modulation" in isolating filters.

The response of the filter can be analyzed following the same framework presented in Section II. Take the filter in Fig. 5 (a) for example, the spectral **ABCD** of the filter is a cascade of the **ABCD** that describe the inverters and the resonators, i.e.,

$$\mathbf{N_2} = \mathbf{N_{J_{S1}}}\mathbf{N_{LC_1}}\mathbf{N_{J_{12}}}\mathbf{N_{LC_2}}\mathbf{N_{J_{2L}}}, \tag{12}$$

where $\mathbf{N_{J_{S1}}}$ and $\mathbf{N_{J_{12}}}$, $\mathbf{N_{J_{2L}}}$ are the spectral **ABCD** matrix of the J-inverters, $\mathbf{N_{LC_1}}$ and $\mathbf{N_{LC_2}}$ are the spectral **ABCD** matrix of the first and second shunt LC resonators, respectively.

To derive the spectral **ABCD** matrix of the inverters in a multi-spectral network (Fig. 2 (b)), we consider the voltage-current relationship of admittance inverters [1]

$$V_{1\pm n} = \pm\frac{1}{jJ}I_{2\pm n}, \tag{13a}$$

$$I_{1\pm n} = \mp jJV_{2\pm n}, \tag{13b}$$

where n refers to the excitation modes into inverters and is defined in the definition of port voltage and current vectors ($\boldsymbol{V_i}$ and $\boldsymbol{I_i}$) in Section II.

Therefore, the spectral **ABCD** matrix of the time-invariant J-inverters can be given as

$$\mathbf{N_J} = \begin{bmatrix} \mathbf{0} & \pm\dfrac{1}{jJ}\mathbf{U} \\ \mp jJ\mathbf{U} & \mathbf{0} \end{bmatrix}. \tag{14}$$

When considering only the carrier frequency, i.e., a time-invariant network, (14) reduces to

$$N_J = \begin{bmatrix} 0 & \pm\dfrac{1}{jJ} \\ \mp jJ & 0 \end{bmatrix},$$

which is the conventional ABCD matrix of J-inverters [1].

Substituting (10) and (14) into (12) gives

$$\mathbf{N_2} = \begin{bmatrix} \dfrac{J_{2L}\mathbf{Y_{LC_1}}}{jJ_{S1}J_{12}} & \dfrac{\mathbf{Y_{LC_1}}\mathbf{Y_{LC_2}} + J_{12}^2\mathbf{U}}{jJ_{S1}J_{12}J_{2L}} \\ \dfrac{J_{S1}J_{2L}\mathbf{U}}{jJ_{12}} & \dfrac{J_{S1}\mathbf{Y_{LC_2}}}{jJ_{12}J_{2L}} \end{bmatrix}. \tag{15}$$

To give a numerical design example, we start with a static 2-pole filter with a 0.043-dB Chebyshev response, 150 MHz
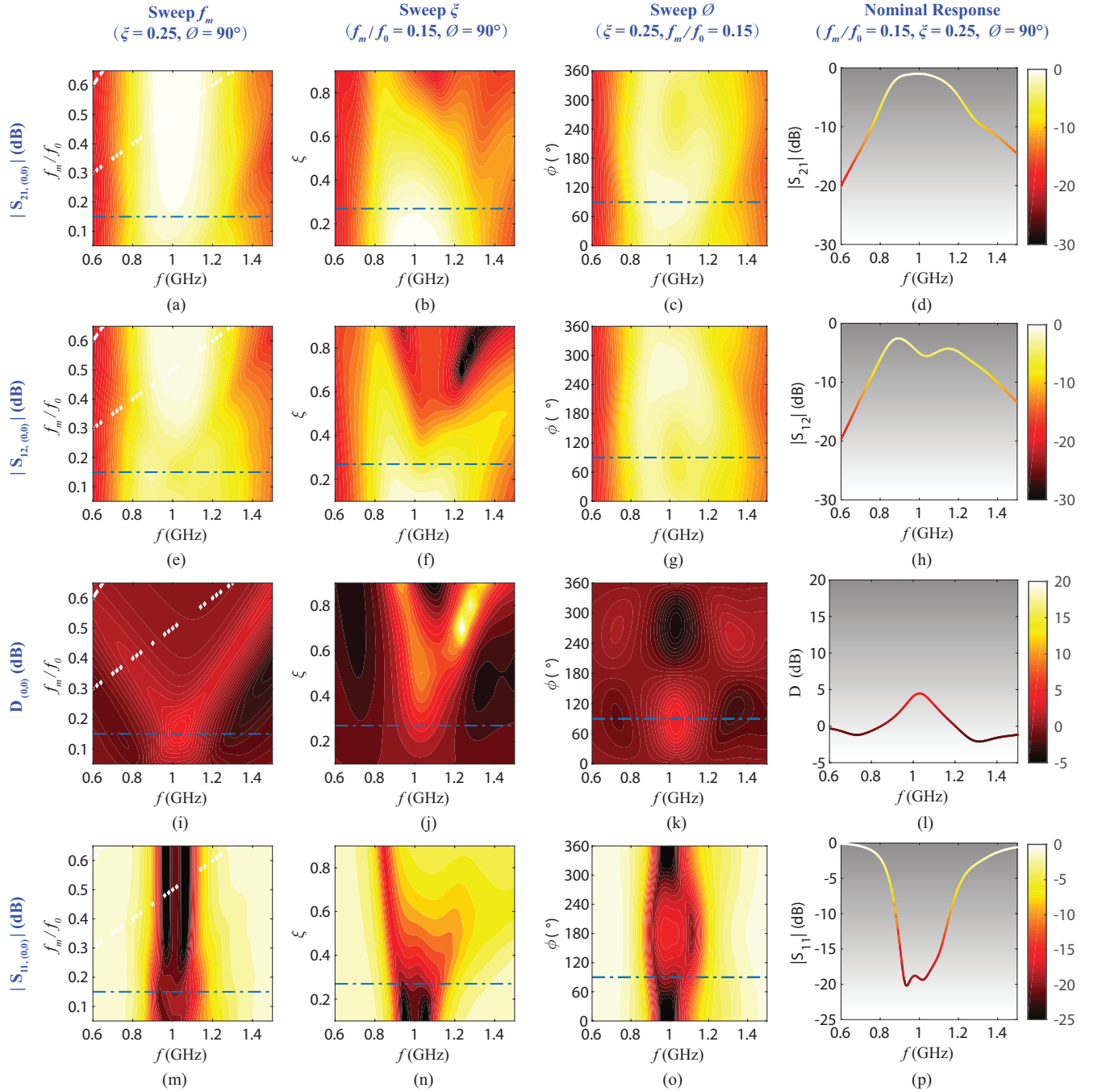
Fig. 6. Parametric studies of 2nd-order filter (the blue dash dot line is to mark the nominal responses in the parametric studies). (a) Modulated $|S_{21,(0,0)}|$ with varied f_m. (b) Modulated $|S_{21,(0,0)}|$ with varied ξ. (c) Modulated $|S_{21,(0,0)}|$ with varied ϕ. (d) Synthesized $|S_{21,(0,0)}|$ with $f_m = 0.15f_0$, $\xi = 0.25$, and $\phi = 90°$. (e) Modulated $|S_{12,(0,0)}|$ with varied f_m. (f) Modulated $|S_{12,(0,0)}|$ with varied ξ. (g) Modulated $|S_{12,(0,0)}|$ with varied ϕ. (h) Synthesized $|S_{12,(0,0)}|$ with $f_m = 0.15f_0$, $\xi = 0.25$, and $\phi = 90°$. (i) Modulated $D_{(0,0)}$ with varied f_m. (j) Modulated $D_{(0,0)}$ with varied ξ. (k) Modulated $D_{(0,0)}$ with varied ϕ. (l) Synthesized $D_{(0,0)}$ with $f_m = 0.15f_0$, $\xi = 0.25$, and $\phi = 90°$. (m) Modulated $|S_{11,(0,0)}|$ with varied f_m. (n) Modulated $|S_{11,(0,0)}|$ with varied ξ. (o) Modulated $|S_{11,(0,0)}|$ with varied ϕ. (p) Synthesized $|S_{11,(0,0)}|$ with $f_m = 0.15f_0$, $\xi = 0.25$, and $\phi = 90°$.

equal-ripple bandwidth (3-dB bandwidth of $350\,\mathrm{MHz}$), and a normalized center frequency of $1\,\mathrm{GHz}$ (Fig. 5 (b)). In the time-varying case, for simplicity, the two resonators are modulated with the same modulation index and modulation frequency, but with different modulation phase. Since only the phase difference is of significance here, ϕ_1 is set to 0 and ϕ_2 is set to be $\Delta\phi$.

It is observed from Fig. 5 (b) that when $\xi = 0$, i.e., there is no modulation, the calculated filter response from (15) agrees exactly with the simulated static response. Next, the frequency response of the 2-pole filter is studied by changing the modulation parameters f_m, ξ, and $\Delta\phi$. The results of the study are shown in Fig. 6. The first three columns of Fig. 6 show the calculated filter frequency response with respect to

$$\mathbf{N_3} = \mathbf{N_{J_{S1}}} \mathbf{N_{LC_1}} \mathbf{N_{J_{12}}} \mathbf{N_{LC_2}} \mathbf{N_{J_{23}}} \mathbf{N_{LC_3}} \mathbf{N_{J_{3L}}}$$

$$= \begin{bmatrix} \dfrac{J_{3L}J_{12}^2\mathbf{U} + J_{3L}\mathbf{Y_{LC1}Y_{LC2}}}{J_{S1}J_{12}J_{23}} & \dfrac{J_{23}^2\mathbf{Y_{LC1}} + J_{12}^2\mathbf{Y_{LC3}} + \mathbf{Y_{LC1}Y_{LC2}Y_{LC3}}}{J_{S1}J_{12}J_{23}J_{3L}} \\[3ex] \dfrac{J_{S1}J_{3L}\mathbf{Y_{LC2}}}{J_{12}J_{23}} & \dfrac{J_{S1}J_{23}^2\mathbf{U} + J_{S1}\mathbf{Y_{LC2}Y_{LC3}}}{J_{12}J_{23}J_{3L}} \end{bmatrix}. \tag{16}$$

f_m, ξ, and ϕ, respectively. The fourth column shows the calculated filter frequency responses for the nominal values of $f_m = 0.15f_0$, $\xi = 0.15$, and $\Delta\phi = 90°$. The four rows of Fig. 6 show $|S_{21,(0,0)}|$, $|S_{12,(0,0)}|$, $D_{(0,0)}$, and $|S_{11,(0,0)}|$, respectively. Here, $D_{(0,0)}$ is defined as $D_{(0,0)} = S_{21}(\text{dB}) - S_{12}(\text{dB})$ to quantify the level of magnitude non-reciprocity at the carrier frequency, which implies the directivity of the isolating filters.

The modulated filter exhibits same-frequency non-reciprocity under most combinations of f_m, ξ, and $\Delta\phi$. With respect to f_m (first column of Fig. 6), it is observed that the modulated filter exhibits the strongest $D_{(0,0)}$ (approximately 5 dB at 1 GHz) when f_m is approximately the same as the equi-ripple bandwidth (150 MHz) of the filter. At this f_m, the $S_{21,(0,0)}$ maintains the filter shape reasonably well with a minimum insertion loss of 0.6 dB. Increasing f_m improves the insertion loss at the cost of $D_{(0,0)}$.

With respect to the modulation index ξ, it is observed that a smaller ξ results in better insertion loss. This is expected as the filter approaches the static design as ξ decreases to 0. Although $D_{(0,0)}$ reaches a very high value of approximately 20 dB for $\xi > 0.6$, the corresponding insertion loss degrades too much to make it a practical design. As shown in Fig. 6 (b), ξ should be kept roughly less than 0.3 to maintain decent insertion loss. A conceptual explanation for this value relates the modulation to the filter's bandwidth. At a capacitance modulation depth of 0.3, the "instantaneous" resonant frequency of a modulated resonator is $\sqrt{1.3} \sim 1.15$ times of its static resonate frequency. At a center frequency of 1 GHz in this example, this instantaneous frequency deviation is approximately a full bandwidth. As such, significant attenuation is presented to the carrier signal, causing a large degradation in the insertion loss. Thus, ξ should be kept relatively small, e.g., around 0.25 to maintain the filter frequency response with low loss.

Not surprisingly, the $S_{21,(0,0)}$ and $S_{12,(0,0)}$ are odd symmetric with respect to each other around the $\phi = 180°$ line. As a result, $D_{(0,0)}$ also exhibits odd symmetry with respect to $\phi = 180°$. When the two resonators are modulated in-phase ($\phi = 0$ or $360°$) or out-of-phase ($\phi = 180°$), $D_{(0,0)}$ is 0 dB, i.e., the modulated filter is reciprocal at the carrier frequency. However, the modulation translates part of the carrier power to the IM frequencies, resulting in a high insertion loss of approximately 5 dB. Maximum $D_{(0,0)}$ and low insertion loss is achieved when ϕ is around $90°$.

At the nominal values of the modulation parameters, a good compromise between the insertion loss, return loss, and non-reciprocity is achieved (the forth column of Fig. 6). Nevertheless, it is evident that a 2-pole filter cannot achieve

both high $D_{(0,0)}$ and good RF performance. We postulate that a better response can be achieved by adding more time-varying components so that more degrees of freedom can be utilized to convert the power at the IM frequencies back to the transmission of the carrier frequency.

C. An Isolating 3-Pole Bandpass Filter

In this Section, we extend the study to a 3-pole filter. We demonstrate that forward transmission $S_{21,(0,0)}$, reflection $S_{11,(0,0)}$, and reverse isolation $S_{12,(0,0)}$ can be achieved simultaneously with high directivity $D_{(0,0)}$.

Fig. 7 (a) shows the circuit topology of the 3-pole STM filter. The three resonators are modulated through time-varying capacitors, which are defined the same as in (11) with $i = 1, 2, 3$ corresponding to the three resonators, respectively. The spectral $\mathbf{ABCD}$ matrix of the filter $\mathbf{N_3}$ can be derived following the same framework as for (12) and it is shown in (16). It should be noted that the same analysis can also be carried out for n-th order filter network.

In this example, the 3-pole filter is designed for the same static specifications as the 2-pole filter presented in Section III-B, namely, a normalized center frequency of 1 GHz, a ripple level of 0.043 dB, and an equi-ripple bandwidth of 150 MHz (3-dB bandwidth of 231 MHz).

Parametric studies on the modulation parameters f_m, ξ, and ϕ are carried out and the results are shown in Fig. 7. The general behavior of the 3-pole STM filter follows those of the 2-pole filter. However, a few distinguishing features in the 3-pole STM filter are worth a discussion.

As shown in the first column of Fig. 7, when f_m is larger than $0.3f_0$, both $|S_{21,(0,0)}|$ and $|S_{12,(0,0)}|$ are close to 0 dB, and the return loss is better than 20 dB with three deep reflection zeros across the passband. The filter is reciprocal at the RF center frequency. A similar behavior is actually observed in the 2-pole filter, but is more evident here. A conceptual explanation for this observation is that for large f_m, the IM frequencies ($\omega \pm n\omega_m$) falls outside of the filter bandwidth and the signal power translated to these frequencies is very small. As such, $S_{21,(0,0)}$ contains very little contribution from the frequency translated components, and little non-reciprocity is observed.

When f_m is smaller than $0.25f_0$, we start observing transmission zeros outside of the passband. These transmission zeros help improve the out-of-band rejection in the forward transmission characteristic of the filter. At the same time, the reflection zero number in the return loss reduces from 3 to 2, and eventually to 1, with a corresponding decrease in
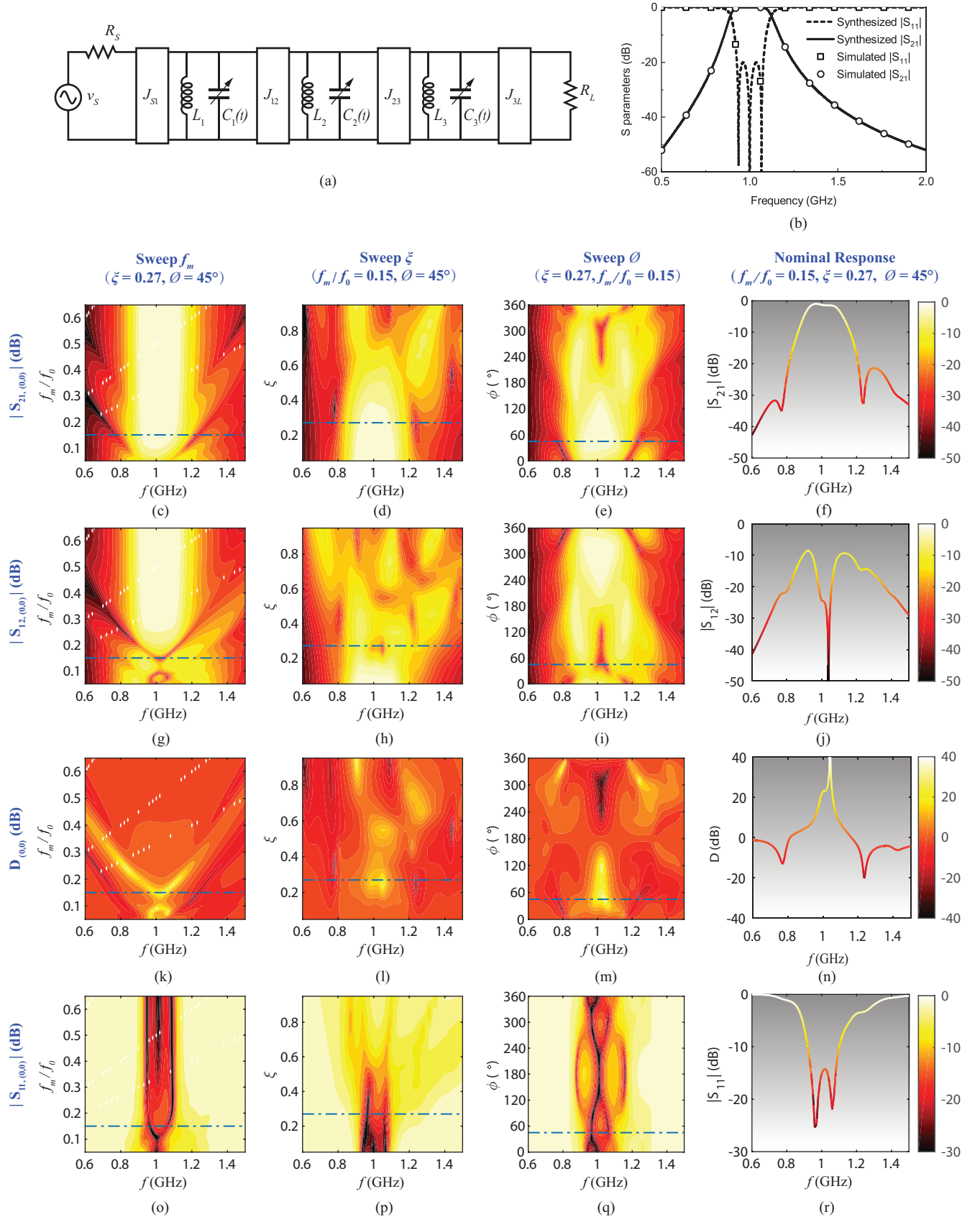
Fig. 7. Parametric studies of 3-pole filter ($J_{S1} = J_{3L} = 0.0119\,\Omega^{-1}$, $J_{12} = J_{23} = 0.0062\,\Omega^{-1}$, $R_S = R_L = 50\,\Omega$, $L_0 = 4\,\text{nH}$, static capacitor value $C_0 = 6.37\,\text{pF}$). (a) Circuit topology of 3-pole filter. (b) Circuit responses without modulation. (c) Modulated $|S_{21,(0,0)}|$ with varied f_m. (d) Modulated $|S_{21,(0,0)}|$ with varied ξ. (e) Modulated $|S_{21,(0,0)}|$ with varied ϕ. (f) Synthesized $|S_{21,(0,0)}|$ with $f_m = 0.15 f_0$, $\xi = 0.27$, and $\phi = 45°$. (g) Modulated $|S_{12,(0,0)}|$ with varied f_m. (h) Modulated $|S_{12,(0,0)}|$ with varied ξ. (i) Modulated $|S_{12,(0,0)}|$ with varied ϕ. (j) Synthesized $|S_{12,(0,0)}|$ with $f_m = 0.15 f_0$, $\xi = 0.27$, and $\phi = 45°$. (k) Modulated $D_{(0,0)}$ with varied f_m. (l) Modulated $D_{(0,0)}$ with varied ξ. (m) Modulated $D_{(0,0)}$ with varied ϕ. (n) Synthesized $D_{(0,0)}$ with $f_m = 0.15 f_0$, $\xi = 0.27$, and $\phi = 45°$. (o) Modulated $|S_{11,(0,0)}|$ with varied f_m. (p) Modulated $|S_{11,(0,0)}|$ with varied ξ. (q) Modulated $|S_{11,(0,0)}|$ with varied ϕ. (r) Synthesized $|S_{11,(0,0)}|$ with $f_m = 0.15 f_0$, $\xi = 0.27$, and $\phi = 45°$.

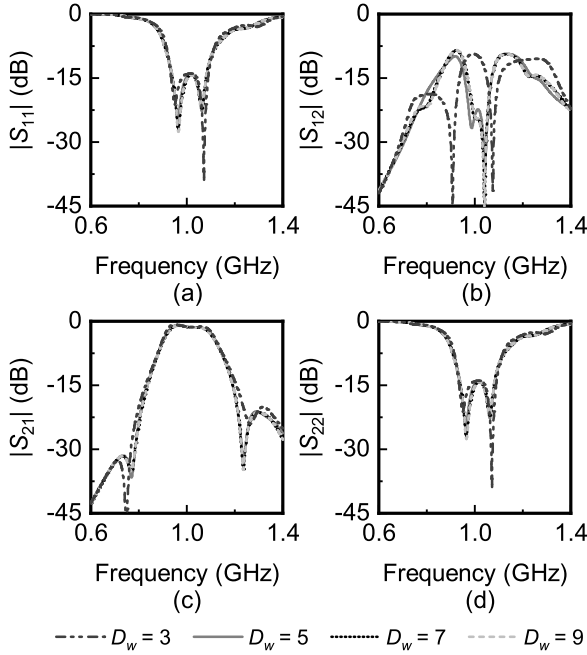Fig. 8. Numerical results with increased dimensions of spectral matrix $\boldsymbol{\omega}$: (a) $|S_{21}|$. (b) $|S_{12}|$. (c) $|S_{11}|$. (d) $|S_{22}|$. $D_{\boldsymbol{\omega}}$ is defined as the dimensions of the spectral frequency matrix. $\omega \pm \omega_m$ and ω are contained for $D_{\boldsymbol{\omega}} = 3$; $\omega \pm 2\omega_m$, $\omega \pm \omega_m$, and ω are contained for $D_{\boldsymbol{\omega}} = 5$; $\omega \pm 3\omega_m$, $\omega \pm 2\omega_m$, $\omega \pm \omega_m$, and ω are contained for $D_{\boldsymbol{\omega}} = 7$; $\omega \pm 4\omega_m$, $\omega \pm 3\omega_m$, $\omega \pm 2\omega_m$, $\omega \pm \omega_m$, and ω are contained for $D_{\boldsymbol{\omega}} = 9$.
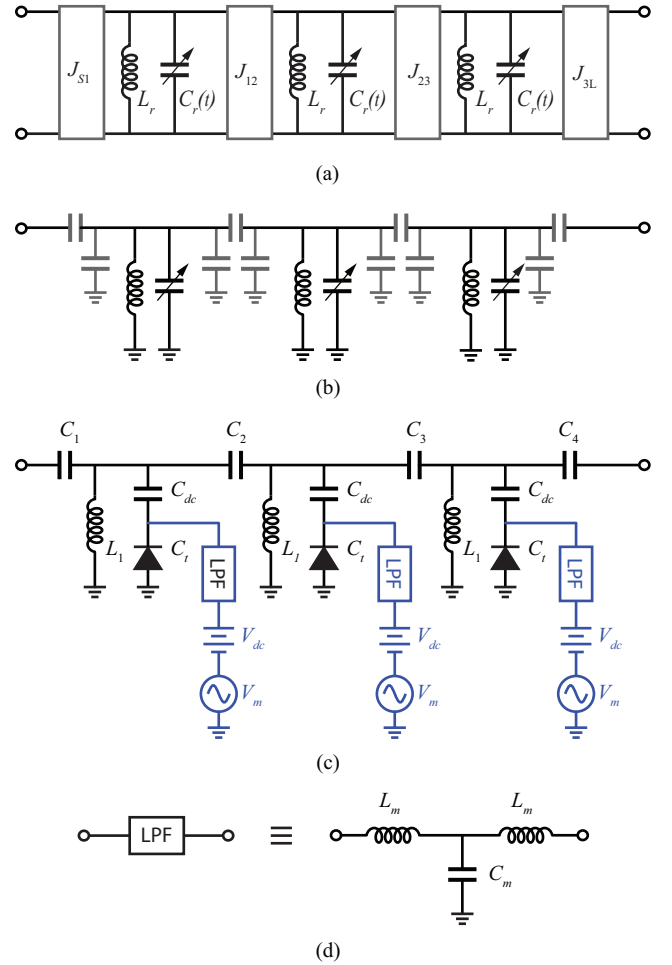

Fig. 9. (a) Circuit topology of 3-pole isolating filter. (b) LC implementation of the 3-pole isolating filter. (c) Practical circuit implementation of 3rd isolating filter with varactors. (d) Bias LPF circuit.

the return-loss bandwidth. A good compromise is reached at $f_m = 0.15 f_0$.

Similar to the 2-pole case, a large modulation index ξ causes significant degradation in the insertion loss. A moderate value of $\xi = 0.27$ results in low insertion loss and good reverse isolation across the equal-ripple bandwidth.

The 3-pole STM filter also exhibits similar behavior as in the 2-pole case with respect to $\Delta\phi$. An odd symmetric $D_{(0,0)}$ profile is observed with respect to $\Delta\phi = 180°$. Compared to the 2-pole case, a much stronger $D_{(0,0)}$ can be observed for $\Delta\phi$ in the range of $30°$–$120°$. A nominal value of $\Delta\phi = 45°$ is chosen for a widest bandwidth over which $D_{(0,0)}$ is maximized.

After the numerical studies above, to have maximum isolation and good filter performance, the modulation parameters f_m, ξ, and ϕ are $0.15 f_0$, 0.27, and $45°$, respectively.

The plots in the forth column of Fig. 7 show the 3-pole STM filter responses. The filter has a center frequency of $1\,\text{GHz}$, a minimum insertion loss of $1\,\text{dB}$, and a 3-dB bandwidth of $205\,\text{MHz}$. The reverse isolation is better than $25\,\text{dB}$. The return loss across the passband is better than $15\,\text{dB}$.

D. Numerical convergence

Theoretically, the IM products in a time-varying network are infinite and therefore would lead to an infinite dimensional full spectral matrix. However, since the signal power is contained within low-order spectral frequencies, the matrix can be truncated to increase numerical efficiency while keeping high

accuracy. Taking 3-pole filter for an example, Fig. 8 shows the numerical results with varied number of spectral frequencies. As the dimensions of spectral matrix increased from 3 to 7, the numerical power transmission and reflection curves differ much, implying unconverged results. When the spectral matrix dimension increases to 7, the results tends to be stable and converged. The numerical studies also reveal that for 3-pole time-varying circuit, most of the signal power is constrained within $\omega \pm 3\omega_m$ since the transmission and reflection curves becomes stable with the spectral matrix dimension increased to be 7. The spectral matrix dimensions are truncated to be 3 and 5 for the single time-varying capacitor in Section II and 2-pole filter in Section III-B, respectively. An extended conclusion can be deduced that for n-pole time-varying filtering network, the spectral matrix can be reduced to be $(2n+1) \times (2n+1)$ without losing numerical accuracy, where n is the variable defined in the voltage and current vectors in Section II.

In summary, more than 1 time-varying circuit component is needed to achieve non-reciprocity on the RF carrier frequency. A minimal example of a 2-pole filter with 2 capacitors modulated with a difference in phase demonstrates the existence of non-reciprocity. However, to achieve practical RF perfor-

TABLE I
LIST OF 3-POLE ISOLATING FILTER DESIGN PARAMETERS

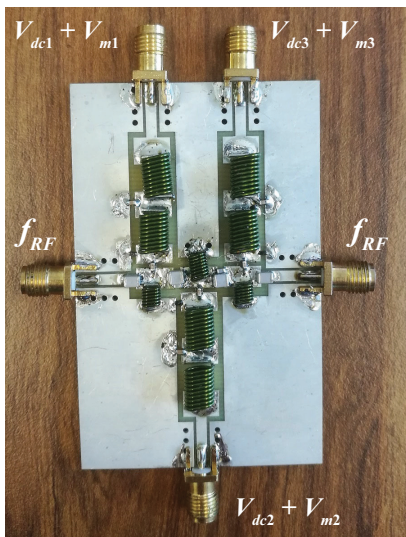| Parameters		Value	Part #
Ideal Filter	f_0	200 MHz	–
	Ripple	0.043 dB	–
	BW_r	30 MHz	–
	BW_{3dB}	46 MHz	–
	L_r	47 nH	–
	C_r	13.2 pF	–
	$J_{S1}\&J_{3L}$	0.0077	–
	$J_{12}\&J_{23}$	0.0026	–
	ξ	0.25	–
	$\Delta\phi$	45°	–
Implementation	$L_1\&L_3$	47 nH	1111SQ-47N (Coilcraft)
	L_2	68 nH	1515SQ-68N (Coilcraft)
	C_{dc}	82 pF	251R14S820JV4S (Johanson)
	C_t	3.8–27 pF	SMV1236 (Skyworks)
	$C_1\&C_4$	8.2 pF	1111N8R3BW501 (PPI)
	$C_2\&C_3$	2.4 pF	1111N2R4BW501 (PPI)
	L_m	180 pH	2222SQ-181 (Coilcraft)
	C_m	82 pF	251R14S820JV4S (Johanson)
	f_m	30 MHz	–
	$\Delta\phi$	70°	–

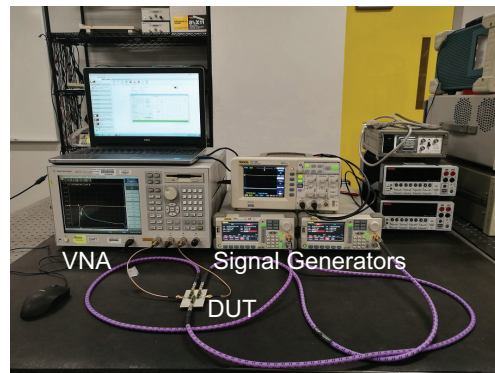Fig. 10. A picture of the fabricated lumped-element 3-pole isolating filter.

Fig. 11. Experimental demonstration of the isolating bandpass filter.
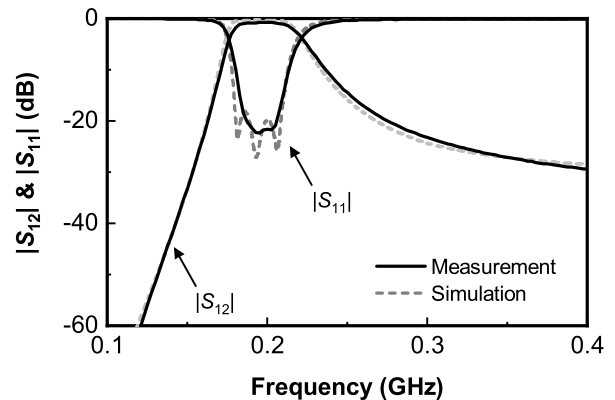

Fig. 12. Simulated and measured non-modulated results.

resonators $\Delta\phi$ should be chosen in the range of 30°–120°. Due to the complexity of the circuits, a numerical optimization or parameter study is inevitable to reach a good balance of the insertion loss, return loss, and isolation.

IV. EXPERIMENTAL VALIDATION

To validate the theory and the design strategy of isolating filters, a 3-pole isolating filter is experimentally demonstrated in this section. The filter is designed for a 0.043 dB Chebyshev response with a center frequency of 200 MHz and a static equal-ripple bandwidth of $BW_r = 30$ MHz. By the design guidelines, the required f_m would be approximately 30 MHz. The filter specifications are chosen according to the availability of the modulating voltage sources.

Fig. 9 shows the evolution of the filter schematic from an ideal design (Fig. 9 (a)) to a physical implementation using lumped components (Fig. 9 (c) and (d)). Each ideal admittance inverter between the resonators is implemented by three capacitors arranged in a Π topology (Fig. 9 (b) [1]. The inverters facing the source and the load impedances are implemented by capacitive dividers/transformers. All the shunt capacitors are absorbed into the resonators, resulting in unequal capacitance of the three resonators. Note that the capacitive networks are narrow-band approximations of the ideal inverters. However, since most of the signal power is contained within $f_0 \pm 3f_m$, where f_m is approximately

mances in terms of insertion loss, return loss, and isolation, higher-order filters are needed to create sufficient degrees of freedom for the frequency translated signals to be converted back to the carrier frequency. An example 3-pole isolating filter shows that much better RF performance can be achieved when compared to the 2-pole filter.

A general design procedure for the proposed isolating bandpass filters starts with the design of a proper static filter response. For optimum performance, the modulation frequency f_m is chosen to be approximately equal to the filter's equal-ripple bandwidth BW_r. The phase difference between the
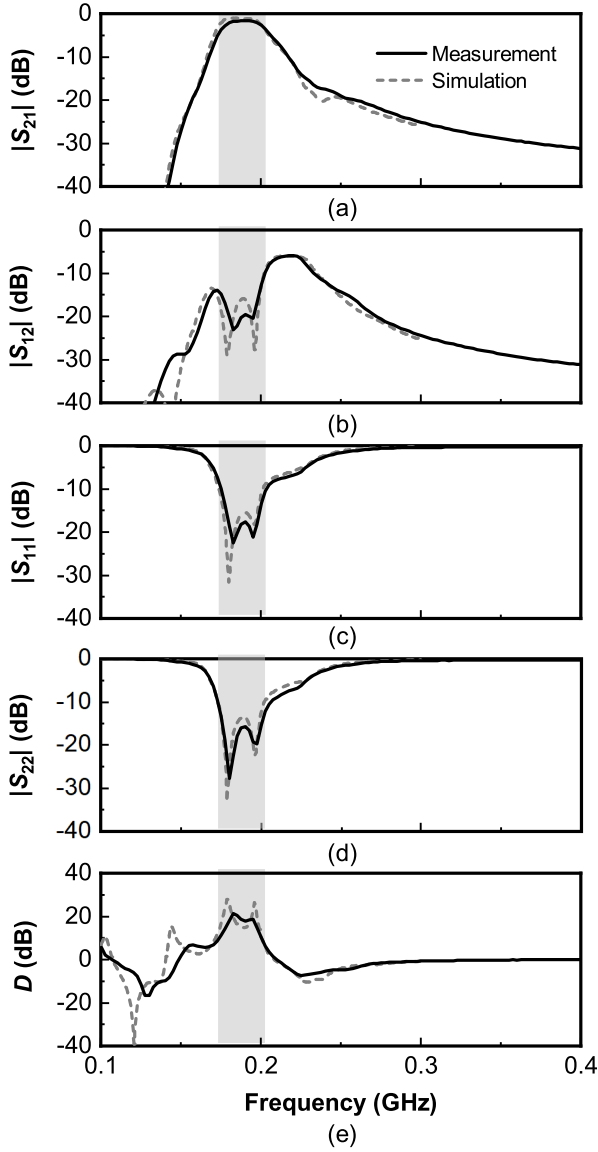
Fig. 13. Simulated and measured modulated responses. (a) Insertion loss $|S_{21}|$. (b) Reverse isolation $|S_{12}|$. (c) Reflection $|S_{11}|$. (d) Reflection $|S_{22}|$. (e) Directivity D.

the filter bandwidth, this approximation does not result in significant degradation in performance.

The ideal time-varying capacitors in (Fig. 9 (b)) are implemented by reverse-biased varactor diodes. To provide the modulation voltage on the varactors, a dc-blocking capacitor C_{dc} is connected in series with the varactor to isolate the shunt inductor from the dc path. The series capacitors of the admittance inverter also serve to isolate the modulation signal f_m from leakage to RF ports. A bias voltage V_{dc} is provided to each varactor to set the nominal capacitance value. A modulation voltage V_m is provided to each varactor with a constant phase shift $\Delta\phi$ between the varactors. V_m is introduced through a low-pass filter (LPF) to further isolate f_m from f_0.

The physical design of the filter is carried out on a 62-mil

FR-4 substrate. The dielectric loss of the FR-4 substrate is not a significant concern in this design due to the relatively low center frequency of 200 MHz. The values and part information of the filter components are listed in Table I. In the design of the filter, realistic models from the component vendors are used to simulate and optimize the filter performance. For example, the parasitics of the SMV1236 varactors (equivalent series resistance $R_s = 0.56\,\Omega$ and series inductance $L_s = 0.7\,\text{nH}$) are included in the simulations. Fig. 10 shows a picture of the fabricated filter.

The measurement setup is shown in Fig. 11. Two dual-channel function generators (Rigol DG5252) are used to supply the modulation voltage V_m with dc offset V_{dc} to the three varactors. A Rigol DS1102E oscilloscope is used to monitor the amplitude and the phase of the modulation voltages. The RF performance is measured with Agilent vector network analyzer E5071A.

Fig. 12 shows the simulated and measured S-parameters when there is no spatio-temporal modulation. The reverse-biased dc voltage on the three varactors are 5.0 V, 4.7 V, and 5.0 V, which give an equivalent static capacitance of 6 pF, 6.3 pF, and 6.0 pF, respectively. It should be noted that the static capacitance of the middle resonator is larger than that of the side resonators to compensate for the absorbed larger negative capacitors in Fig. 9, which well illustrates the evolution of the filter implementation from an ideal design. The static filter exhibits an equal-ripple bandwidth of 29 MHz, a 3 dB bandwidth of 45 MHz (175–220 MHz), and a minimum insertion loss of 0.8 dB. The measurement agrees very well with the simulated dates.

Fig. 13 shows the filter response when STM is introduced. In the measurement, the modulation frequency f_m is set to 28 MHz. As predicted by the studies presented in Section II, f_m is very close to the equal-ripple bandwidth of the filter. The modulation voltages applied on the varactors are 2.4 V, 2.3 V, and 2.4 V, corresponding to capacitance variation of 5.0–10 pF. The modulation phase difference $\Delta\phi$ between the adjacent sources is found to be 45°.

Fig. 13 (a) and (b) show the measured forward transmission S_{21} and backward S_{12} in comparison with the simulation. The filter has a very good forward filtering response with a minimum passband insertion loss of 1 dB in simulation and 1.5 dB in measurement. The measured 3-dB bandwidth covers the frequency range of 170–203 MHz which is slightly smaller than the non-modulated case. Backward S_{12} of the filter has two zeros in the filter's passband, resulting in a directivity D better than 20 dB in the passband (Fig. 13 (e)). The power in the backward direction is spreaded to all the IM frequencies, which are located in the stopband of the filter, most of the converted IM frequencies will be reflected back to port 2. S_{12} in the lower stopband is lower than -15 dB and it almost goes up to -8 dB, differing from the theoretical analysis, which is all bellow -10 dB. It is due to the approximate implementation of ideal frequency-independent coupling (J-inverter), i.e., frequency-dependent capacitive coupling (capacitor). The filter is well matched at both ports showing better than 15 dB of return loss. In all cases, the measurement agrees very well with simulation, validating the effectiveness of the design theory
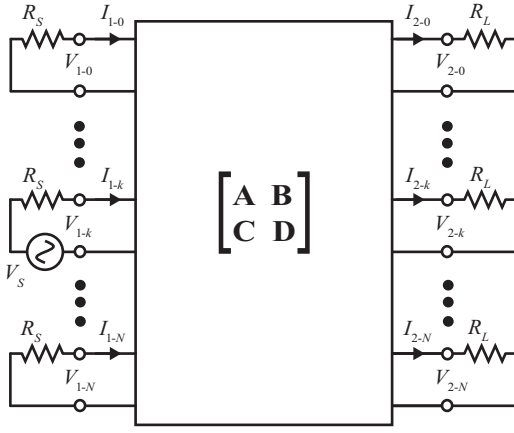
Fig. 14. General multimode circuit with excitation at $k-th$ mode at port 1.

and strategies presented in this paper.

V. CONCLUSIONS

In this paper, we have demonstrated a novel isolating bandpass filter with low-loss forward transmission and high reverse isolation, thus realizing the functions of a bandpass filter and an isolator in one device. The non-reciprocal response is created by modulating the resonators of the filter with an appropriate modulation frequency, modulation index, and phase difference. A spectral domain analysis method is developed to understand the behavior of the circuit. Using this theory, we show that the non-reciprocal frequency conversion due to the modulated resonators is responsible for creating the in-band (same-frequency) non-reciprocity. An isolating bandpass filter example has been demonstrated at a center frequency of $200\,\mathrm{MHz}$ with a forward insertion loss of $1.5\,\mathrm{dB}$ and a reverse isolation of $20\,\mathrm{dB}$ over a bandwidth of $28\,\mathrm{MHz}$. The study presented in this paper opens doors to many interesting non-reciprocal devices and phenomenons in the RF and microwave frequency range.

APPENDIX

The general multimode circuit is given in Fig. 14, where there are N modes at both port 1 and port 2, and an excitation of the k-th mode is connected to the circuit with source impedance R_S, while all the other modes at port 1 are terminated with impedance R_S and all modes at port 2 are terminated with impedance R_L.

$$\begin{bmatrix} V_1^k \\ I_1^k \end{bmatrix} = \begin{bmatrix} \mathbf{A} & \mathbf{B} \\ \mathbf{C} & \mathbf{D} \end{bmatrix} \begin{bmatrix} V_2^k \\ I_2^k \end{bmatrix}, \tag{17}$$

where V_1^k, I_1^k, and V_2^k, I_2^k are spectral vectors at port 1 and port 2, respectively, and the superscript letter k of the ABCD network matrix represents the excitation at k-th mode, where $k = 0, 1, \cdots, N$. In this equation, $\mathbf{A}$, $\mathbf{B}$, $\mathbf{C}$, and $\mathbf{D}$ are the sub-matrices of the network matrix $\mathbf{ABCD}$.

Imposing the boundary conditions, we have

$$V_S^k = I_1^k R_S + V_1^k, \tag{18a}$$
$$V_2^k = I_2^k R_L, \tag{18b}$$

where R_S and R_L are the time-invariant impedance at port 1 and port 2, respectively. $V_S^k = [\cdots, 0, 0, V_S, 0, 0, \cdots]^T$ is a vector whose only non-zero value corresponds to the excitation mode voltage.

From (17) and (18), the following equations can be derived

$$V_S^k = [\mathbf{U} + (\mathbf{A}R_L + \mathbf{B})(\mathbf{C}R_S R_L + \mathbf{D}R_S)^{-1}]R_S I_1^k. \tag{19a}$$
$$V_S^k = (\mathbf{A} + \mathbf{B}/R_L + \mathbf{C}R_S + \mathbf{D}R_S/R_L)V_2^k. \tag{19b}$$

Next, we normalize the equation (19) with the excitation mode voltage V_S, obtaining

$$\overline{V_S^k} = [\mathbf{U} + (\mathbf{A}R_L + \mathbf{B})(\mathbf{C}R_S R_L + \mathbf{D}R_S)^{-1}]R_S(I_1^k/V_S), \tag{20a}$$
$$\overline{V_S^k} = (\mathbf{A} + \mathbf{B}/R_L + \mathbf{C}R_S + \mathbf{D}R_S/R_L)(V_2^k/V_S), \tag{20b}$$

where $\overline{V_S^k} = [\cdots, 0, 0, 1, 0, 0, \cdots]^T$ with only one non-zero value for the k-the element, which identifies the source position. The S parameters can be written as

$$S_{11}^k = \overline{V_S^k} - 2[\mathbf{U} + (\mathbf{A}R_L + \mathbf{B})(\mathbf{C}R_S R_L + \mathbf{D}R_S)^{-1}]^{-1}, \tag{21a}$$
$$S_{21}^k = 2\sqrt{R_L/R_S}(\mathbf{A} + \mathbf{B}/R_L + \mathbf{C}R_S + \mathbf{D}R_S/R_L)^{-1}, \tag{21b}$$

where S_{11}^k is a vector with each element corresponding to the reflection at different mode at port 1 when the excitation is located at the k-th mode at port 1, S_{21}^k is a vector with each element corresponding to the transmission at different mode at port 2 when the excitation is located at the k-th mode at port 1.

Then the spectral $\mathbf{S}$ parameter for the multiple mode circuit is defined as

$$\mathbf{S_{11}} = [S_{11}^0, \cdots, S_{11}^k, \cdots, S_{11}^N], \tag{22a}$$
$$\mathbf{S_{21}} = [S_{21}^0, \cdots, S_{21}^k, \cdots, S_{21}^N]. \tag{22b}$$

Substituting (21) into (22) yields

$$\mathbf{S_{11}} = \mathbf{U} - 2[\mathbf{U} + (\mathbf{A}R_L + \mathbf{B})(\mathbf{C}R_S R_L + \mathbf{D}R_S)^{-1}]^{-1}, \tag{23a}$$

$$\mathbf{S_{21}} = 2\sqrt{\frac{R_S}{R_L}}[\mathbf{A} + \mathbf{B}/R_L + \mathbf{C}R_S + \mathbf{D}R_S/R_L]^{-1}. \tag{23b}$$

Following the same procedure, the spectral $\mathbf{S}$ parameter $\mathbf{S_{22}}$ and $\mathbf{S_{12}}$ can be derived as

$$\mathbf{S_{22}} = \mathbf{U} - 2[\mathbf{U} + (\mathbf{A}R_L + \mathbf{C}R_S R_L)^{-1}(\mathbf{B} + \mathbf{D}R_S)]^{-1}. \tag{24}$$

$$\mathbf{S_{12}} = 2[\mathbf{U} + (\mathbf{A}R_L + \mathbf{B})(\mathbf{C}R_L + \mathbf{D})^{-1}/R_S]^{-1} \times [\mathbf{A} - (\mathbf{A}R_L + \mathbf{B})(\mathbf{C}R_L + \mathbf{D})^{-1}\mathbf{C}]. \tag{25}$$

Thus the spectral $\mathbf{S}$ parameter matrix for the multiple mode circuit is derived. For the conventional dual port network under

single mode situation (N=1), the S parameter matrix in (24) and (25) becomes

$$S_{11} = \frac{A + B/R_L - CR_S - DR_S/R_L}{A + B/R_L + CR_S + DR_S/R_L}, \tag{26a}$$

$$S_{21} = \frac{2}{A + B/R_L + CR_S + DR_S/R_L}, \tag{26b}$$

$$S_{22} = \frac{-A + B/R_L - CR_S + DR_S/R_L}{A + B/R_L + CR_S + DR_S/R_L}, \tag{26c}$$

$$S_{12} = \frac{2(AD - BC)}{AR_L/R_S + B/R_S + CR_L + D}, \tag{26d}$$

which is exactly the same as given in [1].

References

[1] D. M. Pozar, *Microwave Engineering*. Wiley, 2012.

[2] D. Bharadia, E. McMilin, and S. Katti, "Full duplex radios," in *Proceedings of the ACM SIGCOMM 2013 Conference on SIGCOMM*, ser. SIGCOMM '13. New York, NY, USA: ACM, 2013, pp. 375–386.

[3] J. Zhou, N. Reiskarimian, J. Diakonikolas, T. Dinc, T. Chen, G. Zussman, and H. Krishnaswamy, "Integrated full duplex radios," *IEEE Communications Magazine*, vol. 55, no. 4, pp. 142–151, April 2017.

[4] N. Reiskarimian, M. B. Dastjerdi, J. Zhou, and H. Krishnaswamy, "Analysis and design of commutation-based circulator-receivers for integrated full-duplex wireless," *IEEE Journal of Solid-State Circuits*, vol. 53, no. 8, pp. 2190–2201, Aug 2018.

[5] A. Kord, D. L. Sounas, and A. Alú, "Achieving full-duplex communication: Magnetless parametric circulators for full-duplex communication systems," *IEEE Microwave Magazine*, vol. 19, no. 1, pp. 84–90, Jan 2018.

[6] C. Caloz, A. Alù, S. Tretyakov, D. Sounas, K. Achouri, and Z.-L. Deck-Léger, "Electromagnetic nonreciprocity," *Phys. Rev. Applied*, vol. 10, p. 047001, Oct 2018. [Online]. Available: https://link.aps.org/doi/10.1103/PhysRevApplied.10.047001

[7] C. E. Fay and R. L. Comstock, "Operation of the ferrite junction circulator," *IEEE Transactions on Microwave Theory and Techniques*, vol. 13, no. 1, pp. 15–27, Jan 1965.

[8] C. K. Seewald and J. R. Bray, "Ferrite-filled antisymmetrically biased rectangular waveguide isolator using magnetostatic surface wave modes," *IEEE Transactions on Microwave Theory and Techniques*, vol. 58, no. 6, pp. 1493–1501, June 2010.

[9] D. R. Taft, G. R. Harrison, and L. R. Hodges, "Millimeter resonance isolators utilizing hexagonal ferrites," *IEEE Transactions on Microwave Theory and Techniques*, vol. 11, no. 5, pp. 346–356, September 1963.

[10] Y. Konishi, "Lumped element circulators," *IEEE Transactions on Magnetics*, vol. 11, no. 5, pp. 1262–1266, Sep 1975.

[11] S. A. Oliver, P. Shi, N. E. McGruer, C. Vittoria, W. Hu, H. How, S. W. McKnight, and P. M. Zavracky, "Integrated self-biased hexaferrite microstrip circulators for millimeter-wavelength applications," *IEEE Transactions on Microwave Theory and Techniques*, vol. 49, no. 2, pp. 385–387, Feb 2001.

[12] S. Tanaka, N. Shimomura, and K. Ohtake, "Active circulators: The realization of circulators using transistors," *Proceedings of the IEEE*, vol. 53, no. 3, pp. 260–267, March 1965.

[13] Y. Ayasli, "Field effect transistor circulators," *IEEE Transactions on Magnetics*, vol. 25, no. 5, pp. 3242–3247, Sept 1989.

[14] J. Chang, J. Kao, Y. Lin, and H. Wang, "Design and analysis of 24-ghz active isolator and quasi-circulator," *IEEE Transactions on Microwave Theory and Techniques*, vol. 63, no. 8, pp. 2638–2649, Aug 2015.

[15] T. Kodera, D. L. Sounas, and C. Caloz, "Magnetless nonreciprocal metamaterial (MNM) technology: Application to microwave components," *IEEE Transactions on Microwave Theory and Techniques*, vol. 61, no. 3, pp. 1030–1042, March 2013.

[16] G. Carchon and B. Nanwelaers, "Power and noise limitations of active circulators," *IEEE Transactions on Microwave Theory and Techniques*, vol. 48, no. 2, pp. 316–319, Feb 2000.

[17] D. L. Sounas, J. Soric, and A. Alú, "Broadband passive isolators based on coupled nonlinear resonances," *Nature Electronics*, vol. 1, pp. 113–119, February 2018.

[18] Z. Yu and S. Fan, "Complete optical isolation created by indirect interband photonic transitions," *Nature Photonics*, vol. 3, p. 91, January 2008.

[19] H. Lira, Z. Yu, S. Fan, and M. Lipson, "Electrically driven nonreciprocity induced by interband photonic transition on a silicon chip," *Phys. Rev. Lett.*, vol. 109, p. 033901, Jul 2012.

[20] D. Correas-Serrano, J. S. Gómez-Díaz, D. L. Sounas, Y. Hadad, A. Álvarez Melcón, and A. Alú, "Nonreciprocal graphene devices and antennas based on spatiotemporal modulation," *IEEE Antennas and Wireless Propagation Letters*, vol. 15, pp. 1529–1532, 2016.

[21] S. Qin, Q. Xu, and Y. E. Wang, "Nonreciprocal components with distributedly modulated capacitors," *IEEE Transactions on Microwave Theory and Techniques*, vol. 62, no. 10, pp. 2260–2272, Oct 2014.

[22] R. Fleury, D. L. Sounas, C. F. Sieck, M. R. Haberman, and A. Alù, "Sound isolation and giant linear nonreciprocity in a compact acoustic circulator," *Science*, vol. 343, no. 6170, pp. 516–519, 2014.

[23] C. Sounas, Dimitrios L.and Caloz and A. Alú, "Giant non-reciprocity at the subwavelength scale using angular momentum-biased metamaterials," *Nature Communications*, vol. 4, p. 2407, Sep 2013.

[24] N. A. Estep, D. L. Sounas, J. Soric, and A. Alú, "Magnetic-free nonreciprocity and isolation based on parametrically modulated coupled-resonator loops," *Nature Physics*, vol. 10, pp. 923–927, Dec 2014.

[25] N. A. Estep, D. L. Sounas, and A. Alú, "Magnetless microwave circulators based on spatiotemporally modulated rings of coupled resonators," *IEEE Transactions on Microwave Theory and Techniques*, vol. 64, no. 2, pp. 502–518, Feb 2016.

[26] A. Kord, D. L. Sounas, and A. Alú, "Magnet-less circulators based on spatiotemporal modulation of bandstop filters in a delta topology," *IEEE Transactions on Microwave Theory and Techniques*, vol. 66, no. 2, pp. 911–926, Feb 2018.

[27] M. M. Torunbalci, T. J. Odelberg, S. Sridaran, R. C. Ruby, and S. A. Bhave, "An fbar circulator," *IEEE Microwave and Wireless Components Letters*, vol. 28, no. 5, pp. 395–397, May 2018.

[28] C. Xu, E. Calayir, and G. Piazza, "Magnetic-free electrical circulator based on aln mems filters and cmos rf switches," in *2018 IEEE Micro Electro Mechanical Systems (MEMS)*, Jan 2018, pp. 755–758.

[29] A. Kord, D. L. Sounas, and A. Alú, "Pseudo-linear time-invariant magnetless circulators based on differential spatiotemporal modulation of resonant junctions," *IEEE Transactions on Microwave Theory and Techniques*, vol. 66, no. 6, pp. 2731–2745, June 2018.

[30] Y. Yu, G. Michetti, A. Kord, D. Sounas, F. V. Pop, P. Kulik, M. Pirro, Z. Qian, A. Alú, and M. Rinaldi, "Magnetic-free radio frequency circulator based on spatiotemporal commutation of mems resonators," in *2018 IEEE Micro Electro Mechanical Systems (MEMS)*, Jan 2018, pp. 154–157.

[31] A. Kord, D. L. Sounas, Z. Xiao, and A. Al, "Broadband cyclic-symmetric magnetless circulators and theoretical bounds on their bandwidth," *IEEE Transactions on Microwave Theory and Techniques*, vol. 66, no. 12, pp. 5472–5481, Dec 2018.

[32] M. M. Biedka, R. Zhu, Q. M. Xu, and Y. E. Wang, "Ultra-wide band non-reciprocity through sequentially-switched delay lines," *Scientific Reports*, vol. 7, p. 40014, Jan 2017.

[33] N. Reiskarimian and H. Krishnaswamy, "Magnetic-free non-reciprocity based on staggered commutation," *Nature Communications*, vol. 7, p. 11217, Apr 2016.

[34] N. Reiskarimian, J. Zhou, and H. Krishnaswamy, "A cmos passive lptv nonmagnetic circulator and its application in a full-duplex receiver," *IEEE Journal of Solid-State Circuits*, vol. 52, no. 5, pp. 1358–1372, May 2017.

[35] A. Nagulu, T. Dinc, Z. Xiao, M. Tymchenko, D. L. Sounas, A. Al, and H. Krishnaswamy, "Nonreciprocal components based on switched transmission lines," *IEEE Transactions on Microwave Theory and Techniques*, vol. 66, no. 11, pp. 4706–4725, Nov 2018.

[36] T. Dinc, M. Tymchenko, A. Nagulu, D. Sounas, A. Alú, and H. Krishnaswamy, "Synchronized conductivity modulation to realize broadband lossless magnetic-free non-reciprocity," *Nature Communications*, vol. 8, p. 795, Oct 2017.

[37] M. D. Hickle, "Synthesis, design, and fabrication techniques for reconfigurable microwave and millimeter-wave filters," *Ph.D. dissertation, School Elect. Comput. Eng., Purdue Univ., West Lafayette, IN, USA*, 2016.

[38] C. Kurth, "Steady-state analysis of sinusoidal time-variant networks applied to equivalent circuits for transmission networks," *IEEE Transactions on Circuits and Systems*, vol. 24, no. 11, pp. 610–624, Nov 1977.